A novel laser vision sensor for weld line detection on wall-climbing robot

CrossMark

Liguo Zhang, Wei Ke, Qixiang Ye [1], Jianbin Jiao *

School of Electronics, Electrical and Communication Engineering, University of Chinese Academy of Sciences, Beijing 100049, China

A B S T R A C T

In this paper, we present a cross-structure light (CSL) sensor, that consists a structured light projector and a camera, for weld line detection. The structured light projector projects cross laser beams on the weldment to form cross stripes, which are captured in images by a CCD camera for measurement. We use feature points, a planar target and a homograph matrix to calibrate the sensor. We also propose an effective approach to extract laser stripes in images for weld line detection. Experiments show that the CSL sensor can capture 3D information of the weldment with very low measurement error, and the weld line detection approach is effective in wall-climbing robotic platform navigation.

© 2014 Elsevier Ltd. All rights reserved.

1. Introduction

To perform non-destructive testing very important to guarantee the safety operation of lots of industry facilities, such as towers of the wind turbines and oil storage tanks. In automatic non destructive testing (NDT) systems, automatic weldline detection and tracking can navigate moving platforms and improve the testing performance and efficiency significantly.

In literature, distance measurement [1,2], monocular vision [3,4] and structured light some approaches have been applied to detect the weld lines [5,6]. Distance measurement method usually uses the distance sensor arrays to obtain depth estimates of points reflecting the convexity shape of excess weld metal on the weld line. However, the depth points are discrete although distance sensor arrays have complex mechanical structures. In addition, depth information is invisible, which makes it difficult to operate the system when manual intervention is required. Monocular vision approaches are simpler and more intuitive than those based on distance sensor arrays, however, it is often difficult to obtain the 3D information of weldment surface by a single camera. Moreover, weld lines on painted surface often have similar color with their background, which makes it difficult to distinguish the weld lines from their background.

Laser structured light sensors have attracted more and more attentions and are widely used in robot areas, such as automatic welding [7,8], industry inspection [9–11], 3D measurement [12,13], quality control [14], and robot navigation [15–17], for its simplicity, noncontact and strong anti-interference abilities. It is observed that most of the weld lines have weld convexity formed in the welding process. Structured light that can capture these convex shapes with a visible manner is introduced to detect and track weld line.

In terms of the laser projected patterns, the system normally projects a laser spot, a single laser stripe, or multiple laser stripes. More patterns like a circle, concentric multiple circles and a grid are also used. In industrial environment, for instance, the single laser stripe is widely used for weld seam detection in welding process. Unlike weld seam detection, weld line detection includes detecting T-intersection between horizontal and vertical weld lines of tanks and towers; therefore, single laser stripe is unsuitable for the weld line detection. In order to solve this problem, a cross laser stripe-based structured light sensor is presented in this paper.

In our weld line detection and tracking system, a CSL sensor is designed to project a red cross laser beam on the weldment surface to form a cross laser stripe which is then captured by a CCD camera. The laser stripe projected by CSL can reflect the height of weld convexity, detect horizontal and vertical weld lines simultaneously and be insensitive to illumination changes. The CCD camera captures 20 color video frames per second in H.264 format with resolution of 640×480. Captured video sequences are transmitted to PC with a wireless module for weld line detection and tracking. The operations of detection and tracking are performed on PC. Detected and tracking results will be transmitted

* Corresponding author.
E-mail addresses: zhangliguo08@mails.ucas.ac.cn (L. Zhang),
kewei11@mails.ucas.ac.cn (W. Ke), Qxye@ucas.ac.cn (Q. Ye),
jiaojb@ucas.ac.cn (J. Jiao).
[1] Q. Ye has been a visiting Assistant Professor of University of Maryland since 2012.
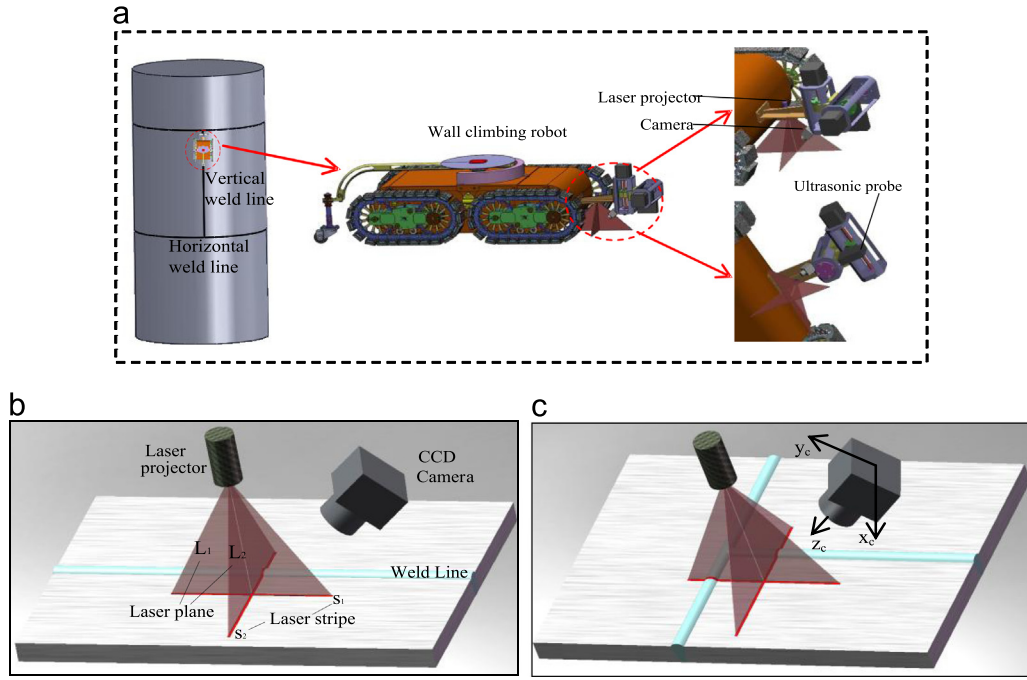
Fig. 1. Weld line detection and tracking system. (a) The platform. (b)The CSL projector and imaging CCD on straight weld line, and (c) on cross weld lines.

Table 1
Configuration of the CSL sensor.

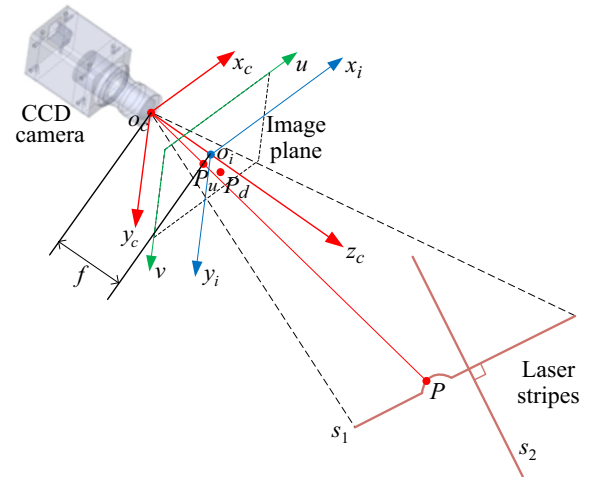| Device	Parameters
Camera	CCD: SONY: 1/4 in.
	Resolution: 640×480 pixel
	Pixel size: 5.6 μm $\times$ 5.6 μm
	Frame rate: 20 fps
	Focal length:8 mm
	Field of view: 43.7°
Laser projector	Size:ϕ 9 $\times$ 23 mm
	Wavelength: 635 nm
	Operating voltage: DC 5 V
	Operating current: 20–50 Ma
	Output power: 5 mW
	Fan angle: 60°

Fig. 2. Measurement model of the CSL sensor.

back to robot to feed into a PID controller and then converted into the Cartesian space of robot end-effecter frame to control its movement. The controller is described in [18] and the weld line localization is described in [6]. The details of both are omitted in this paper.

The remainder of this paper is organized as follows. In Section 2, the model of the CSL sensor is introduced. In Section 3, the approaches of extracting the laser stripe and localizing sub-pixel location are presented. In Section 4, the calibration approach for the CSL sensor is described. We present calibration experiments and actual measurement experiments of the sensor in Section 5 and conclude the paper in Section 6.

2. Model of CSL sensor

Our weld line detection and tracking system platform is shown in Fig. 1(a). It is composed of a wall-climbing robot, an ultrasonic device of NDT and a CSL sensor. The configuration of the CSL sensor is shown in Table1. Fig. 1(b) and (c) illustrate the CSL projector and image capturing CCD on straight weld line and cross weld lines, respectively. The laser projector is fixed on the robot

and perpendicular to the weldment. Two stripes s_1 and s_2 are formed by intersection lines between weldment and two orthogonal laser planes L_1 and L_2.

The laser projector projects a cross laser beam on the weld line, forming convex light stripe around weld line. According to the laser triangulation measurement method, the 3D information of the weldment surface can be obtained by calculating the camera coordinates of the points on the light stripes transformed from the image coordinates. In general, when the robot moves along the straight weld line, only a convex arc exists on the stripe s_2, as shown in Fig. 1(b). When the robot is close to a T-intersection of vertical and horizontal weld lines, two convex arcs will appear at the strips, as showed in Fig. 1(c). The sensor can simultaneously detect the locations of the horizontal and the vertical weld lines, which are used to plan the motion path of the robot.

According to the above principle, the measurement model of CSL sensor is described in Fig. 2. $o_c-x_cy_cz_c$ is used to describe the camera coordinate system. $o_co_i=f$ denotes the focal length of the camera. $o_ix_iy_i$ denotes the image coordinate system. In camera

coordinate system, two mutually orthogonal laser planes L_1 and L_2 are defined as:

$$a_1 x_c + b_1 y_c + c_1 z_c + 1 = 0 \quad (1)$$

and

$$a_2 x_c + b_2 y_c + c_2 z_c + 1 = 0, \quad (2)$$

respectively, where

$$a_1 a_2 + b_1 b_2 + c_1 c_2 = 0. \quad (3)$$

There is an arbitrary point P on the stripe S_1. $P_c = [x_{cp}, y_{cp}, z_{cp}]^T$ denotes the coordinate of point P in camera coordinate system and $p_u = [x_{up}, y_{up}]^T$ denotes the coordinate of point P in image coordinate system. The image coordinate of p_u is represented by $[u_{up}, v_{up}]^T$. Assuming width and height of a pixel are dx (mm) and dy (mm), respectively, in image coordinate system the transformational relation from millimeter coordinate to pixel coordinate is described as

$$\begin{cases} u_{up} - u_0 = x_{up}/dx \\ v_{up} - v_0 = y_{up}/dy \end{cases}. \quad (4)$$

The transformational relation from image coordinate to camera coordinate is described as

$$\begin{bmatrix} u_{up} \\ v_{up} \\ 1 \end{bmatrix} = \begin{bmatrix} k_x & 0 & u_0 \\ 0 & k_y & v_0 \\ 0 & 0 & 1 \end{bmatrix} \begin{bmatrix} x_{cp}/z_{cp} \\ y_{cp}/z_{cp} \\ 1 \end{bmatrix} = K \begin{bmatrix} x_{cp}/z_{cp} \\ y_{cp}/z_{cp} \\ 1 \end{bmatrix}, \quad (5)$$

where $k_x = f/dx$, $k_y = f/dy$. The point $[u_0, v_0]^T$ is the intersection coordinates of the optical axis and the image plane, i.e., principal point of the camera in the image plane. K is the camera's intrinsic matrix.

Actual lenses do not obey the ideal pinhole model due to lens distortion. When modeling CSL sensor, correction of radial distortions and tangential distortions is used to improve the measurement

precision. In Fig. 2 point p_u is the unobservable distortion free image coordinates, and $p_d = [x_d, y_d]^T$ is the corresponding coordinates with distortion correction. p_u and p_d are decided by the positions of the points in the image plane and described with

$$\begin{cases} x_{up} = k_1 x_d(x_d^2 + y_d^2) + k_2 x_d(x_d^2 + y_d^2)^2 + p_1(2x_d^2 + (x_d^2 + y_d^2)) + p_2(2x_d y_d) \\ y_{up} = k_1 y_d(x_d^2 + y_d^2) + k_2 y_d(x_d^2 + y_d^2)^2 + p_2(2y_d^2 + (x_d^2 + y_d^2)) + p_1(2x_d y_d) \end{cases}, \quad (6)$$

where parameters k_1, k_2 are coefficients of radial distortion. The parameters p_1, p_2 represent coefficients of tangential distortion. According to Eqs. (1), (2) and (4)–(6), the camera model and coordinates of points on the laser stripe can be calculated.

## 3. Laser stripe extraction and localization

The result of laser stripe extraction greatly affects the measurement result of a structured light system. Robustness, accuracy and speed are required in the laser stripe positioning process. In general, laser stripe extraction is based on luminance histogram

Table 2
Parameters of the CSL sensor.

Category	Parameters	Physical meaning
Camera intrinsic parameters	(f_x, f_y)	Focal length in the x, y direction
	(u_0, v_0)	Principle point coordinates
	(k_1, k_2)	Radial distortion parameters
	(p_1, p_2)	Tangential distortion parameters
Light plane equations	(a_1, b_1, c_1)	Laser plane L_1 equation coefficients
	(a_2, b_2, c_2)	Laser plane L_2 equation coefficients
	$\angle l_1 o l_2$	Angle between L_1 and L_2
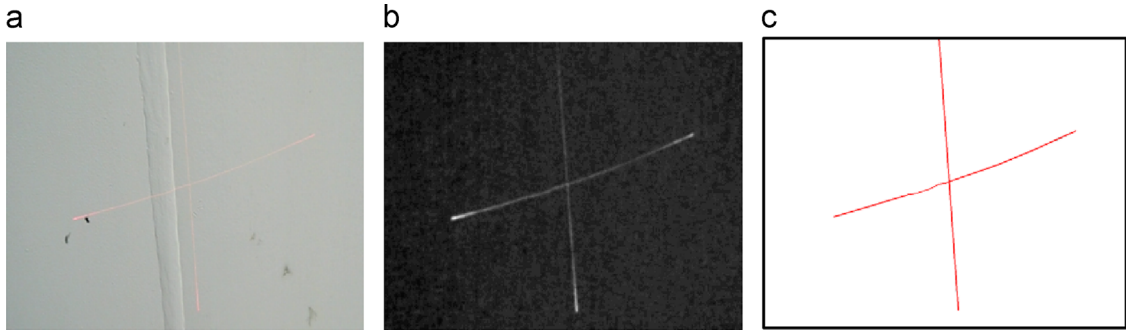
Fig. 3. Laser stripe extraction. (a) Laser stripe under high light. (b) Extraction result. (c) Sub-pixel location of the laser stripe.
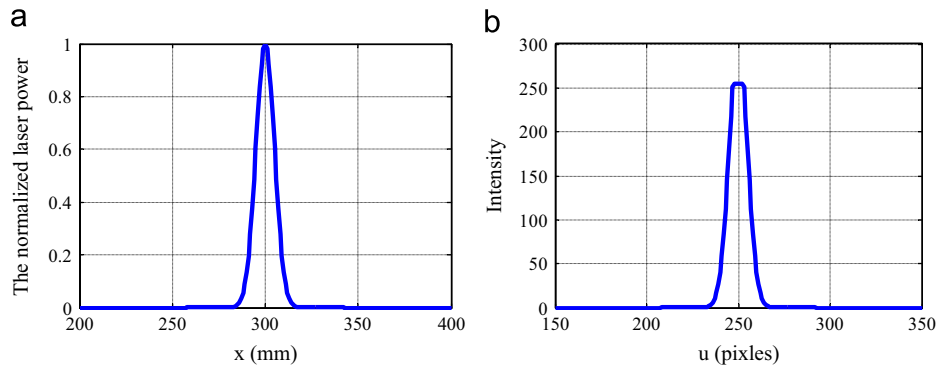
Fig. 4. Characteristics of laser stripe. (a) is the power distribution of a laser stripe's profile and (b) is the intensity discribution in image.

and threshold segmentation method. These methods are simple and fast, but it are sensitive to noise and illumination, especially under bright sunlight in the wild. In real environment with natural light, the background of the stripe in captured image has red, green and blue (RGB) components of similar value. However, on the stripe of the red laser, R component is considerably larger than G or B component because laser is characterized by high brightness and pure monochromaticity. Therefore, we present a new method which makes the illumination different between R and G

or B component in order to extract the laser stripe. For example, a RGB color image captured by camera with 640×480 pixel resolution whose column number and row number are $n=640$ and $m=480$, respectively. Stripe extraction is calculated with

$$I_{i,j} = \max\{|I_{i,j}^R - I_{i,j}^G|, \quad |I_{i,j}^R - I_{i,j}^B|\}, \quad i \in [0, m), \quad j \in [0, n), \tag{7}$$

where $I_{i,j}$ is the pixel value at the ith row, jth column of the image after extracting stripe. The $I_{i,j}^R$, $I_{i,j}^G$ and $I_{i,j}^B$ are R, G and B component values, respectively.

In Fig. 3(a), it can be seen that the stripe of captured image is less clear under high light and the signal-noise-ratio (SNR) is very low. According to Eq. (7), a well extraction result with high SNR is obtained, as shown in Fig. 3(b).

Existing methods of sub-pixel laser stripe localization including geometry center detection [19], energy center calculation [20], maximum intensity value along the cross laser stripe profile and curve fitting algorithm of Gaussian distribution [21]. However, these methods are often sensitive to illumination variations and shadow. On the cross profile of laser stripe, the intensity distribution is approximated to a Gaussian distribution, as shown in Fig. 4(a). But in photosensitive cells of CCD the excessive saturation effect is often posed by the high intensity of laser stripe. Therefore, in a captured image, the profile of stripe is a Gaussian distribution with cutting top distortion, as shown in Fig. 4(b). Under such circumstances,
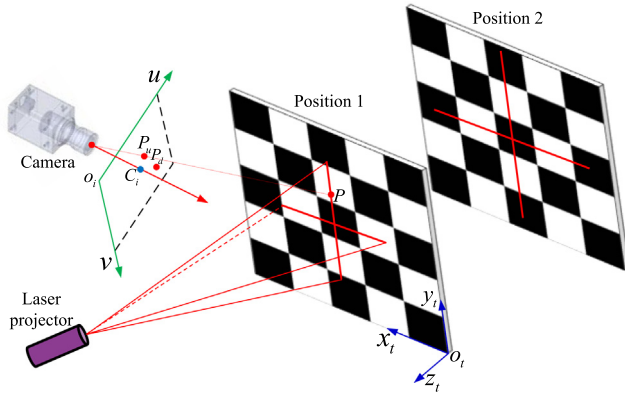

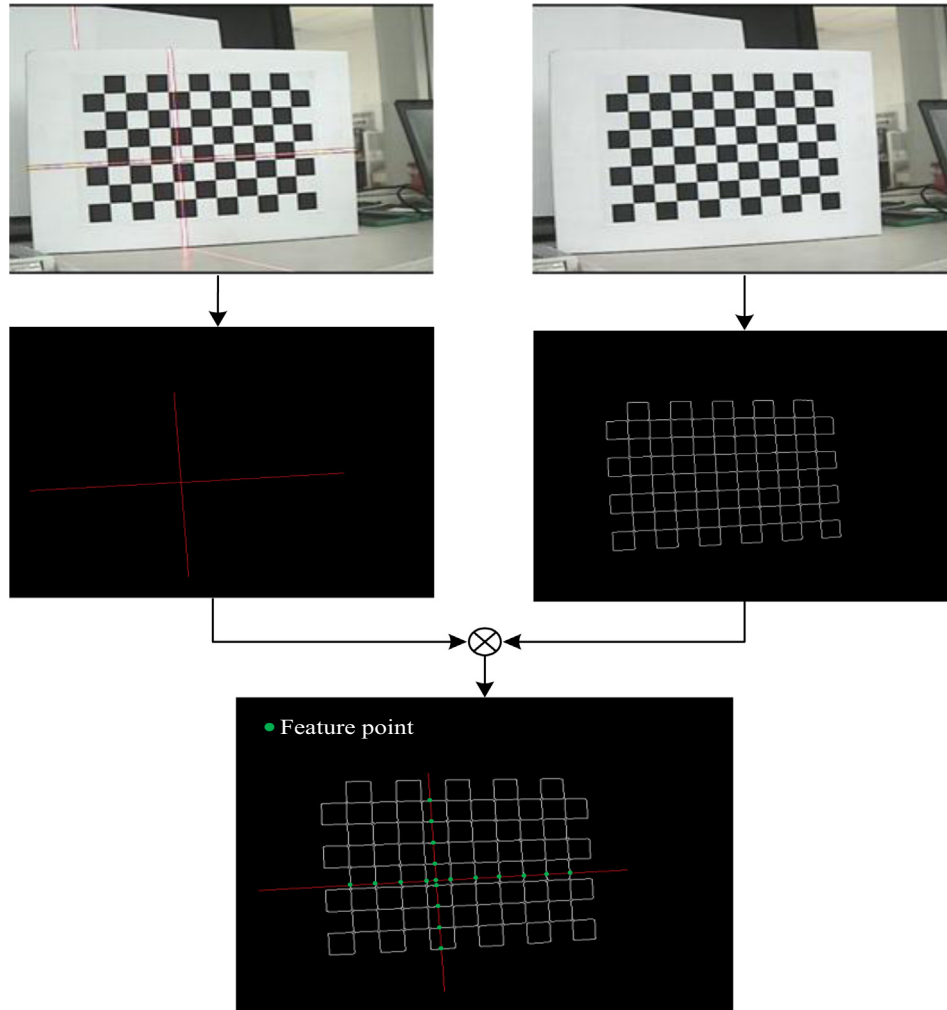
Fig. 5. Sensor calibration.

Fig. 6. Feature point selection. Middle-left: center-of-mass points of the laser stripes. Middle-right: edges of the chessboard. Bottom: Defined feature points (green points). (For interpretation of the references to color in this figure legend, the reader is referred to the web version of this article.)

maximum illumination is more than one point in the profile which will affect calculation of the Gaussian approximation.

A center-of-mass algorithm is used to localize the center line of a stripe. Take a vertical stripe as an example, on the ith row, the center-of-mass is calculated within a small search window around the stripe's maximum intensity. In the profile, a column coordinate of the center-of-mass of ith row, $M_i(w)$, is calculated as follows

$$M_i(w) = \frac{\sum_{j^i_{max}-(w/2)}^{j^i_{max}+(w/2)} I_{i,j} \times j}{\sum_{j^i_{max}-(w/2)}^{j^i_{max}+(w/2)} I_{i,j}}, i \in [0,n), j \in [0,m), \qquad (8)$$

where the maximum light intensity of ith row is jth column, represented by j^i_{max}. w is the size of search window. The stripe width and laser beam brightness affect the value of w. In the experiments, we empirically set the value of w to 9 pixel. Along with the conclusions from [6], we can determine the center line of the extracting stripe shown in Fig. 3(c).

4. CSL sensor calibration

In the sensor calibration process, we need to determine model parameters such as intrinsic, extrinsic and laser planes parameters. Corresponding parameters and physical meanings of these categories are shown in Table 2.

The intrinsic parameters of the camera are calculated using Zhang's method [22], in which a camera observes a planar chessboard target from different perspectives. The camera and the planar chessboard target can move freely and the relative camera positions among different poses are unknown, as shown in Fig. 5. The calibration procedure gives a closed form solution, followed by a nonlinear refinement based on the maximum likelihood criterion.

In Fig. 5 the planar chessboard target is used to calibrate the laser planes. $o_t - x_t y_t z_t$ is a target coordinate system of the target plane and it is used as the world coordinate system. Under this condition, the z coordinates of all points of the target plane equals zero. From a 3D target plane coordinate system to 2D image coordinate system, the translation is given as

$$s\tilde{m} = A[r_1 \quad r_2 \quad r_3 \quad t] \begin{bmatrix} x_t \\ y_t \\ z_t \\ 1 \end{bmatrix} = A[R \quad t]\tilde{M} \qquad (9)$$

Table 3
The calibration results of the CSL sensor.

Parameters	Values
(f_x, f_y)	(922.4350, 917.3560)
(u_0, v_0)	(329.1680, 2705660)
(k_1, k_2)	$(-291.459 \times 10^{-3}, 157.027 \times 10^{-3})$
(p_1, p_2)	$(-0.1354 \times 10^{-3}, -0.2682 \times 10^{-3})$
(a_1, b_1, c_1)	$(-0.18 \times 10^{-3}, 1.86 \times 10^{-3}, 1.39 \times 10^{-3})$
(a_2, b_2, c_2)	$(-90.11 \times 10^{-3}, 2.463 \times 10^{-3}, 8.935 \times 10^{-3})$
$\angle l_1 o l_2$	89.9981°
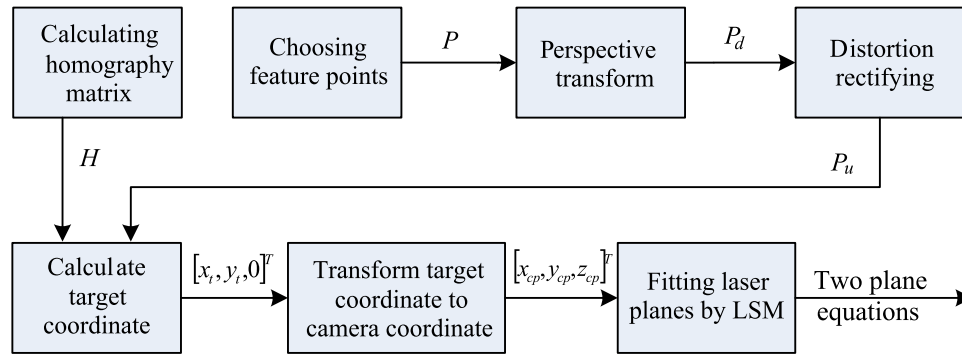
Fig. 7. Flowchart of the feature point coordinate calculation.
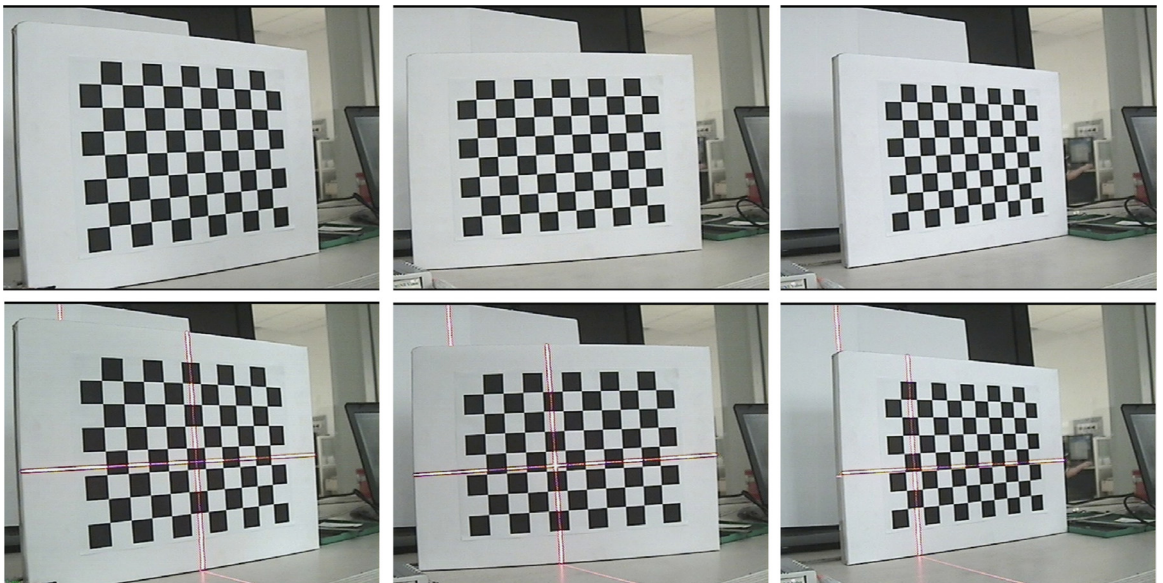
Fig. 8. Calibration chessboard. The chessboards without and with laser stripe are shown on the first and the second row, respectively.

where $\tilde{m} = [u \quad v \quad 1]^T$ is the homogeneous coordinates of $m = [u \quad v]^T$; $\tilde{M} = [x_t \quad y_t \quad z_t \quad 1]^T$ is the homogeneous coordinates of $M = [x_t \quad y_t \quad z_t]^T$ in the 2D target plane; s is an arbitrary scale factor; 3×3 matrix $R = (r_1 \quad r_2 \quad r_3)$ and 3×1 matrix $t = (t_1 \quad t_2 \quad t_3)^T$ are rotation matrix and translation vector between two coordinate systems, respectively. According to $z_t = 0$ on target plane, the translation between $\tilde{m}$ and $\tilde{M}$ is described as

$$\tilde{m} = \frac{1}{s} A [r_1 \quad r_2 \quad t] \tilde{M}' = H \tilde{M}' \tag{10}$$

where homography matrix H is given as $H = [h_1 \quad h_2 \quad h_3]^T$ (h_i, $i = 1$, 2 or 3 is row vector of H); $\tilde{M}' = [x_t \quad y_t \quad 1]^T$. H can be coarsely calculated with Eq. (10) with at least four non-collinear points. Then a maximum likelihood estimation method is used to calculate the accurate H by minimizing the objective function

$$F = \min \sum_i \left\| m_i - \frac{1}{h_3^T M_i} \begin{bmatrix} h_1^T M_i \\ h_2^T M_i \end{bmatrix} \right\|^2 \tag{11}$$

Table 4
Calibration accuracy.

Image coordinates	Intersection with target plane			Intersection with laser plane			Errors of coordinates			Plane
(u,v)/(pixels)	x (mm)	y (mm)	z (mm)	x (mm)	y (mm)	z (mm)	Δx (mm)	Δy (mm)	Δz (mm)	L_i
Position 1										
460.751, 335.462	164.013	−12.358	715.797	164.030	−12.359	715.870	−0.017	0.001	−0.073	L_1
459.293, 302.781	139.099	−11.389	717.654	139.123	−11.391	717.776	−0.024	0.002	−0.122	L_1
457.397, 273.486	114.184	−10.460	719.511	114.219	−10.464	719.737	−0.035	0.004	−0.226	L_1
455.191, 241.971	89.280	−9.292	721.365	89.281	−9.292	721.374	−0.001	0	−0.009	L_1
454.704, 233.089*	82.424	−9.009	721.875	82.424	−9.008	721.875	0	−0.001	0	L_1 L_1
453.134, 211.396	64.365	−8.343	723.222	64.373	−8.344	723.307	−0.008	0.001	−0.085	L_1
450.753, 180.022	39.453	−7.335	725.078	39.458	−7.335	725.160	−0.005	0	−0.082	L_1
448.104, 150.019	14.533	−6.506	726.938	14.539	−6.509	727.258	−0.006	0.003	−0.320	L_1
527.350, 227.396	84.210	53.089	720.774	84.698	53.396	724.948	−0.488	−0.307	−4.174	L_2
499.698, 229.251	83.512	28.097	721.216	83.601	28.127	721.982	−0.089	−0.030	−0.766	L_2
469.536, 231.634	82.794	3.106	721.659	82.681	3.102	720.668	0.113	0.004	0.991	L_2
438.771, 234.059	82.196	−21.891	722.093	82.191	−21.889	722.046	0.005	−0.002	0.047	L_2
409.476, 237.016	81.538	−46.884	722.532	81.593	−46.916	723.015	−0.055	0.032	−0.483	L_2
377.858, 239.002	80.940	−71.881	722.966	80.813	−71.769	721.835	0.127	−0.112	1.131	L_2
346.985, 241.499	80.371	−96.879	723.398	80.045	−96.486	720.462	0.326	−0.393	2.936	L_2
315.000, 243.500	79.683	−121.872	723.839	79.96	−122.295	726.351	−0.277	0.423	−2.512	L_2
283.036, 245.994	79.085	−146.868	724.273	79.359	−147.378	726.784	−0.274	0.510	−2.511	L_2
253.213, 247.974	78.407	−171.861	724.713	78.419	−171.887	724.823	−0.012	0.026	−0.11	L_2
RMS errors (mm)	–	–	–	–	–	–	0.173	0.198	1.526	–
Position 2										
388.505, 328.662	162.480	−102.514	865.645	162.456	−102.500	865.525	0.024	−0.014	0.120	L_1
387.231, 301.868	138.915	−101.188	857.410	138.894	−101.174	857.295	0.021	−0.014	0.115	L_1
385.278, 274.185	115.350	−99.862	849.170	115.332	−99.849	849.060	0.018	−0.013	0.110	L_1
383.796, 246.583*	91.785	−98.536	840.930	91.770	−98.524	840.825	0.015	−0.012	0.105	L_1 L_2
382.084, 218.982	68.220	−97.210	832.690	68.207	−97.199	832.590	0.013	−0.011	0.100	L_1
380.332, 191.419	44.650	−95.884	824.450	44.644	−95.873	824.355	0.006	−0.011	0.095	L_1
378.177, 164.690	21.085	−94.558	816.210	21.081	−94.548	816.120	0.004	−0.010	0.090	L_1
501.055, 240.841	101.140	51.150	838.250	101.144	51.150	838.280	−0.004	0	−0.030	L_2
479.406, 242.050	99.580	26.205	838.695	99.585	26.202	838.735	−0.005	0.003	−0.040	L_2
456.570, 243.119	98.020	1.255	839.140	98.024	1.253	839.180	−0.004	0.002	−0.040	L_2
432.967, 244.302	96.465	−23.694	839.590	96.465	−23.695	839.635	0	0.001	−0.045	L_2
408.778, 245.455	94.905	−48.641	840.035	94.905	−48.644	840.080	0	0.003	−0.045	L_2
357.951, 248.033	93.345	−73.589	840.480	93.345	−73.592	840.520	0	0.003	−0.040	L_2
331.581, 248.972	90.225	−123.483	841.375	90.226	−123.490	841.420	−0.001	0.007	−0.045	L_2
304.445, 250.285	88.665	−148.431	841.820	88.667	−148.440	841.875	−0.002	0.009	−0.055	L_2
276.665, 251.784	87.105	−173.378	842.265	87.107	−173.388	842.315	−0.002	0.010	−0.050	L_2
RMS errors (mm)	–	–	–	–	–	–	0.011	0.009	0.077	–

* Present intersection point of two stripes.
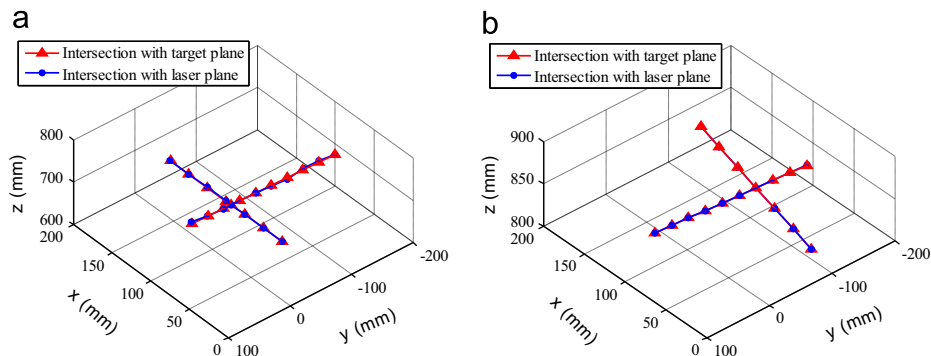
Fig. 9. 3D coordinates of standard values and measured values in the camera coordinate system. (a) Position 1 and (b) Position 2.

where $m_i = \begin{pmatrix} u_i & v_i & 1 \end{pmatrix}^T$ and $M_i = \begin{pmatrix} x_i & y_i & 1 \end{pmatrix}^T$ are the homogeneous coordinates of the *ith* feature point in image coordinate system and its corresponding point in target plane coordinate system, respectively. The minimizing problem can be solved by the Levenberg–Marquardt algorithm [23]. The initial value can be obtained from a linear least squares method.

After the camera calibration, we follow the flowchart shown in Fig. 7 to calculate the equations of the laser planes. On the chessboard, the intersection points of the edges of black/white squares and the laser stripes are defined as feature points. This process aims to extract laser stripes in the chessboard images with laser stripes. For chessboard images without laser stripes, the edges of black/white squares are extracted instead. Then the coordinates of the intersection points are calculated, as shown in Fig. 6. We place the chessboard in different positions to get the camera coordinates of sufficient points on the stripes through the steps of Fig. 7. The space equations of laser planes L_1 and L_2 are fitted using a least square method (LSM).

5. Experiments

5.1. Calibration

A chessboard is used as a target board of camera calibration. On the chessboard, the side length of each black/white square is equal to 25 mm. There are 10×7 corner points on the target board.
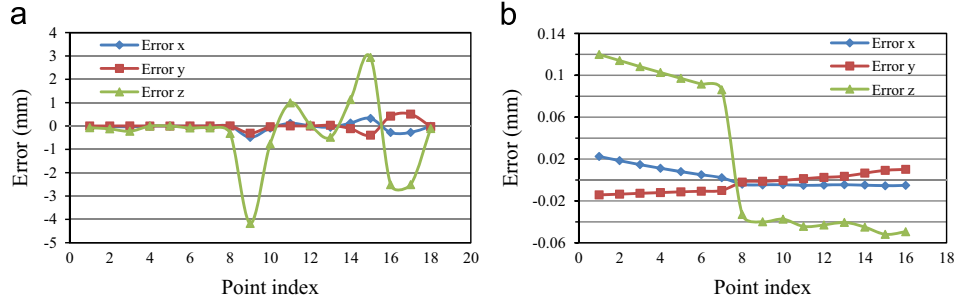
There are 16 captured images of target board in different positions. For each position, an image with laser stripe and an image without laser stripe are captured, respectively, as shown in Fig. 8. The two sets of images are used to calibrate camera and calculate equations of laser planes, respectively. We randomly choose three images in three different positions, and then extract the coordinates of feature points of laser stripe using the method in Section 3. Based on the method described in Section 4, the feature points of camera coordinate system are calculated, and then the equations of laser
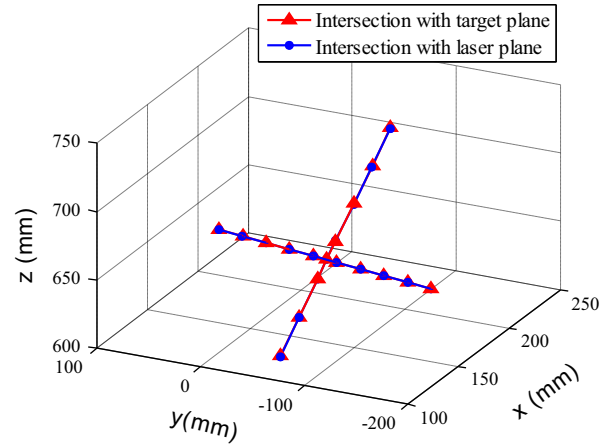

Fig. 11. A3D coordinates of standard values and measured values in Position 3.

Fig. 10. Calibration errors in x, y and z directions. (a) Position 1. (b) Position 2.

Table 5
Measurement accuracy.

| Image coordinates	Intersection with target plane			Intersection with laser plane			Errors of coordinates			Plane index
(u,v)/(pixels)	x (mm)	y (mm)	z (mm)	x (mm)	y (mm)	z (mm)	Δx (mm)	Δy (mm)	Δz (mm)	L_i
Position 3										
434.812, 216.242	224.751	−61.644	713.681	224.542	−61.586	713.015	0.209	−0.058	0.666	L_1
521.702, 339.656	208.124	−60.198	695.059	207.856	−60.121	694.164	0.268	−0.077	0.895	L_1
520.861, 304.699	191.494	−58.802	676.438	191.424	−58.781	676.191	0.07	−0.021	0.247	L_1
519.817, 272.006	174.863	−57.407	657.818	174.962	−57.439	658.187	−0.099	0.032	−0.369	L_1
518.237, 238.050∗	166.850	−56.695	648.842	166.851	−56.695	648.845	−0.001	0	−0.003	L_1,L_2
516.309, 220.555	158.236	−55.971	639.196	158.309	−55.996	639.490	−0.073	0.025	−0.294	L_1
515.171, 204.063	141.610	−54.515	620.575	141.588	−54.507	620.479	0.022	−0.008	0.096	L_1
512.486, 170.342	124.986	−53.019	601.952	124.763	−52.925	600.875	0.223	−0.094	1.077	L_1
508.894, 138.080	177.332	57.495	649.622	177.262	57.472	649.365	0.07	0.023	0.257	L_2
577.181, 225.223	175.097	32.586	649.509	175.014	32.571	649.198	0.083	0.015	0.311	L_2
565.821, 224.684	172.689	7.687	649.202	172.695	7.687	649.225	−0.006	0	−0.023	L_2
554.325, 223.663	170.521	−17.226	649.164	170.473	−17.221	648.984	0.048	−0.005	0.18	L_2
539.553, 223.101	168.219	−42.131	648.977	168.197	−42.126	648.891	0.022	−0.005	0.086	L_2
525.946, 222.546	165.957	−67.039	648.834	165.937	−67.031	648.754	0.02	−0.008	0.08	L_2
510.778, 220.525	163.709	−91.947	648.706	163.683	−91.932	648.602	0.026	−0.015	0.104	L_2
494.025, 219.462	161.487	−116.857	648.608	161.441	−116.823	648.420	0.046	−0.034	0.188	L_2
477.062, 218.398	159.212	−141.763	648.451	159.175	−141.730	648.298	0.037	−0.033	0.153	L_2
457.027, 217.322	156.884	−166.667	648.234	156.884	−166.667	648.235	0	0	−0.001	L_2
RMS errors (mm)	–	–	–	–	–	–	0.107	0.036	0.407	–
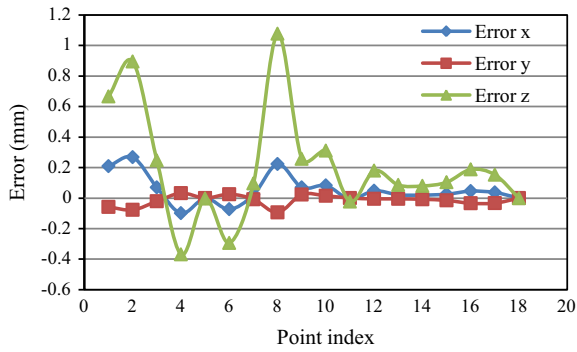
Fig. 12. Measurement errors in three directions in Position 3.

planes are fitted. A plane equation can be obtained by at least 3 non-collinear feature points. The calibration results of the CSL sensor are shown in Table 3.

It can be seen in Table 3 that the dot product of the coefficients of the two plane equations is equal to $a_1a_1+b_1b_2+c_1c_2 = 3.322 \times 10^{-5}$, which is close to zero.

In Table 4 we quantitatively evaluate the calibration accuracy of the sensor by comparing two groups of the camera coordinate system. The values in the first group are the coordinates of intersection points of the target board and rays of light between the optical center and feature points, and are adopted as standard values, as shown in Fig. 5. The values in the second group are measured values, which are the coordinates of the intersection points of the laser planes and rays of light between optical center
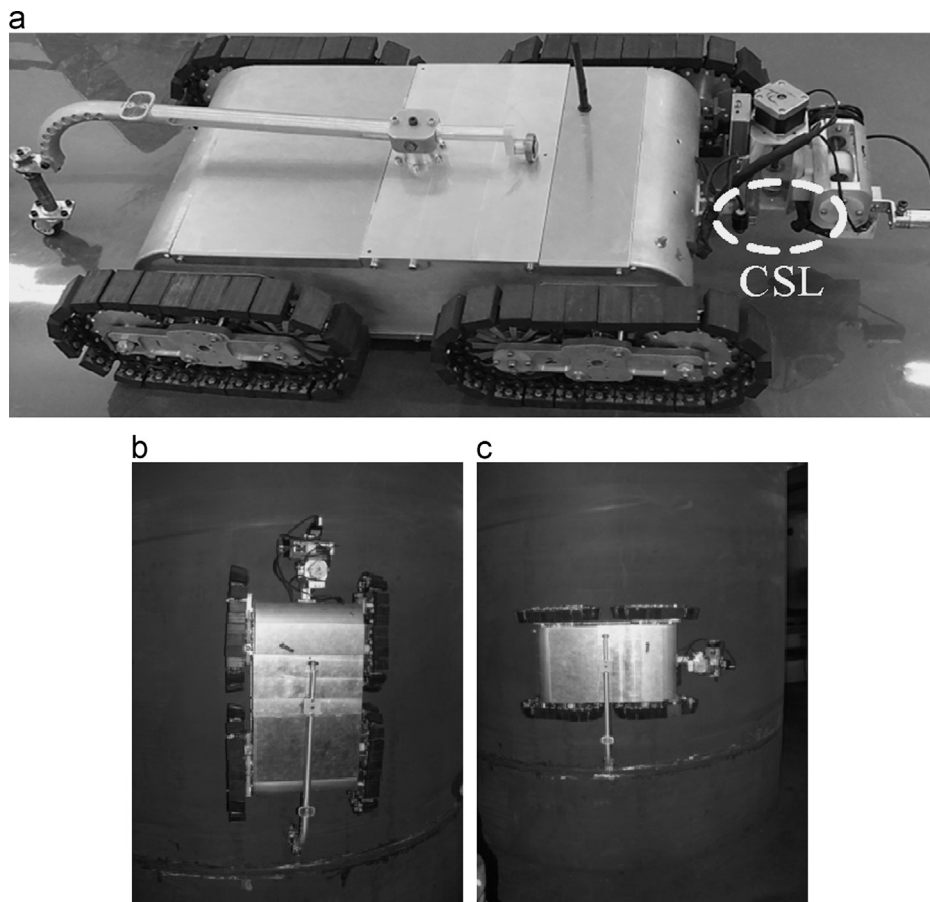

Fig. 13. Wall climbing robot prototype. (a) Robot with the CSL device. (b) Robot working in vertical direction, and (c) Robot working in horizontal direction.
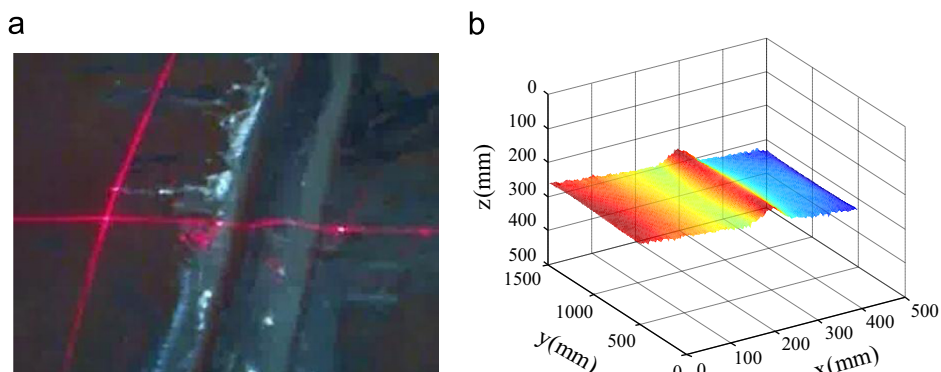

Fig. 14. (a) Straight weld line detection of uneven lighting and weld defects. (b) 3D coordinates of a weld line section.

and feature points. In the first position we select 18 stripe points for calibration. In the second position, 16 points are selected. In *x*, *y* and *z* direction, root-mean-square (RMS) errors of the two group of points are (0.173, 0.198, 1.526) and (0.011, 0.008, 0.077), respectively. Figs. 9 and 10 show 3D space coordinates and calibration errors of the two groups of points. It can be seen that the two groups of points have a high contact ratio and a minor error. From Fig. 10 it can be seen that Δz is larger than Δx and Δy due to the fact that *z* is larger than *x* and *y*.

5.2. Measurement

In the third position, 18 feature points are calculated to evaluate measurement accuracy of the system using the laser plane equations. We obtain RMS errors of (0.107, 0.036, 0.407) in three directions, as listed in Table 5. The difference between Tables 4 and 5 lies in that the data of Table 5 form a new test set. The test set is not used to calibrate the camera and laser planes. The coordinates of feature points in the 3D space are shown in Fig. 11.

Fig. 12 shows the measurement errors. From Figs. 11 and 12 it can be seen that the sensor system has high measurement accuracy.

5.3. Weld line detection

In order to verify the feasibility of the CSL sensor, the calibrated sensor is tested on a tower of the wind turbine by a wall climbing robot platform, as shown in Fig. 13. There two types of weld lines on the tower: straight and T-intersection weld lines, as shown in Figs. 14 and 15(a). The location of the weld line is detected by the method in [6]. According to the detection results, the robot can follow the weld line and perform NDT. When the robot moves close to the T-intersection of the weld lines, as shown in Fig. 15(a), two stripes are used to detect the weld lines. Once the system detects the weld lines, 3D information of the weldment surface is measured with the laser triangulation measurement method. According to the measured values, the control system commands the robot to make a turn.

In Figs. 14 and 15(a), we show the detection and measurement experiments in the wild environment. Under the circumstances
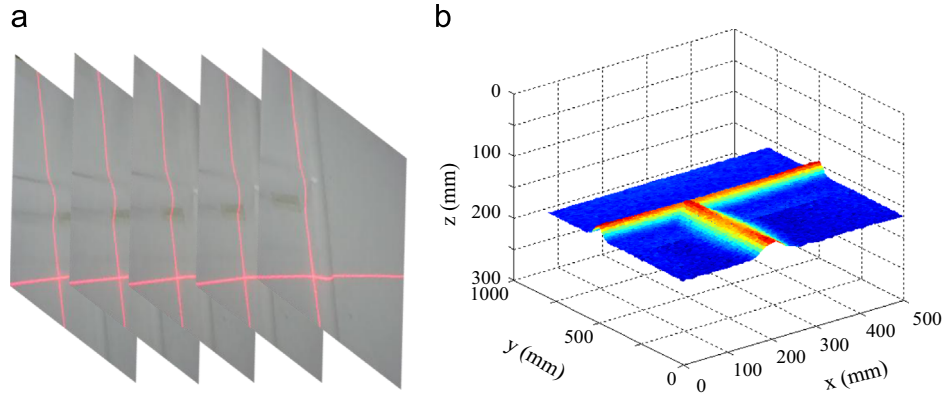

Fig. 15. Measurement results and 3D coordinates of T-intersection weld lines.
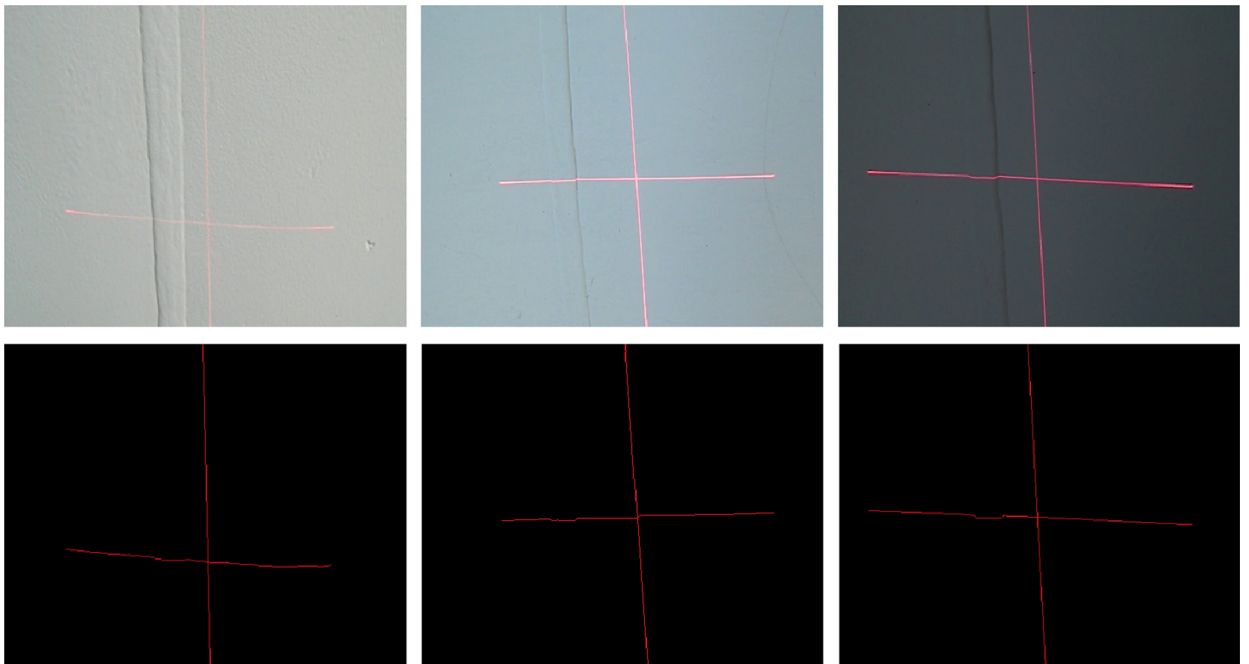

Fig. 16. Laser stripe extraction. The first row contains frames and the second row contains extracted laser stripes of the first row.

of high illumination and excessive noise, the robustness of the sensor stands out. Figs. 14 and 15(b) show the reconstructed 3D surfaces of the weld lines. Fig. 15(a) illustrates the detection results of the T-intersection weld lines and Fig. 15(b) shows the measurement results of the T-intersection weld lines. Both vertical and horizontal weld lines appear in the video sequence. It can be seen that the CSL sensor can detect and measure both vertical and horizontal weld lines when the platform moves close to the intersection part of the two weld lines. The smooth shapes of the detected and tracked weld line (the convex shapes in Fig. 15 (b)) demonstrate the effectiveness of the sensor.

In Fig. 16, we show the laser stripes extraction results in three frames captured in the wild environment. Despite high illumination and varying intensity of light in the frames, our approach exhibits good performance.

When the robot moves along the straight weld lines, the measured weld line locations can be used directly for navigation. When the robot moves close to T-intersection weld lines, we can get two convex arcs on the laser stripes, and the vertical and horizontal locations of the weld lines can be extracted simultaneously using the CSL sensor. If the robot moves from a vertical weld line to a horizontal one, it will turn right. And if the robot moves from a horizontal weld line to a vertical one, it will turn to the vertical weld line, as shown in Fig. 17(a). The green line

represents motion track when the robot is moving upwards along weld line and red line represents motion track when the robot is moving downwards along weld line. In Fig. 17(b) and (c), we show the navigation and motion trajectories of the robot at the T-intersection of the weld lines. Although there are a few isolated detection errors, the robot platform can still move along the weld lines, which demonstrates the accuracy of the CSL sensor.

In this paper, the measured object is the weld line of a wind power tower. The tower is a bulky cone with the height of about 30–50 m and the diameter of about 2.2–4 m. Therefore, the structured light sensor may not reconstruct 3D information of the whole tower as measuring parts. We just reconstruct the local 3D information around the weld line. Fig. 17(d) shows the measured 3D information of a T-intersection of the weld lines.

6. Conclusion

In this paper, we designed a sensor with a cross structured light (CSL) projector and a CCD camera for weld line detection. The projector projects two orthogonal red laser beams onto the weldment surface to form two red stripes which contain the 3D information of weld convexity. The CSL sensor can detect the two types of weld lines: straight and T-intersection weld lines.
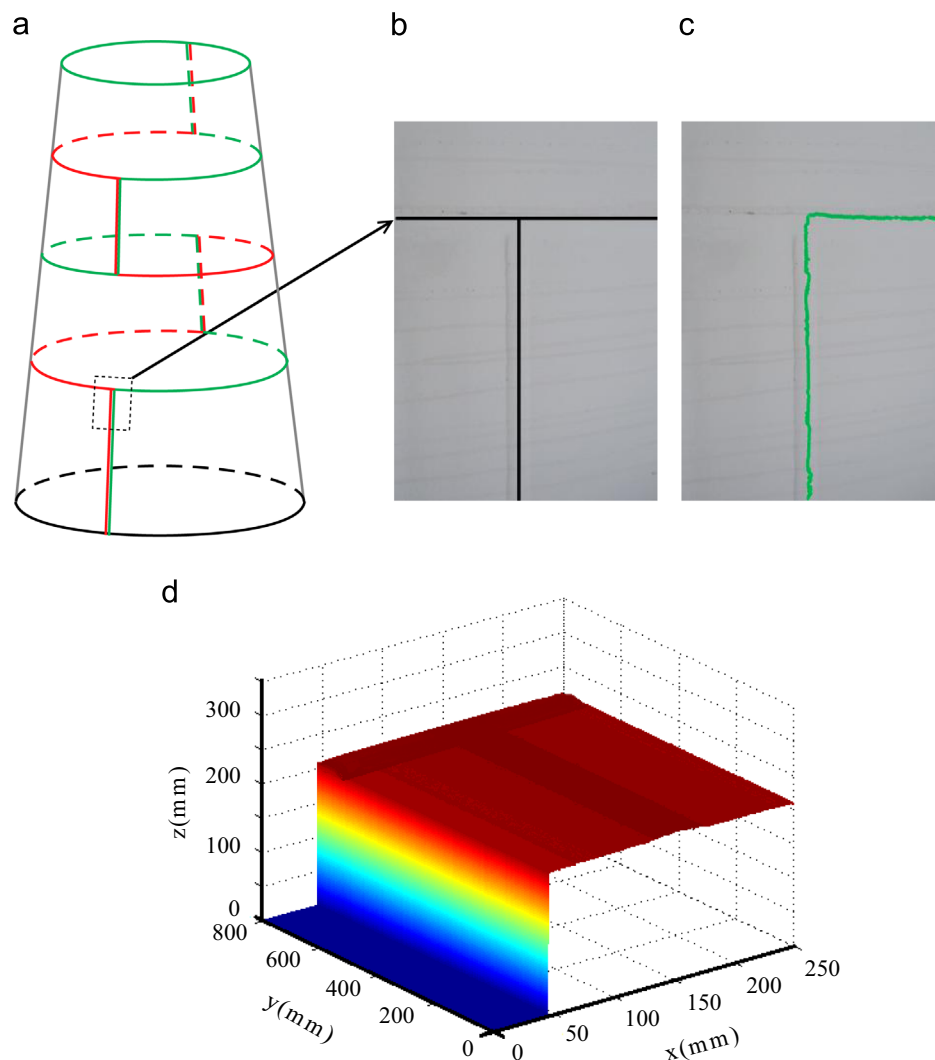
Fig. 17. (a) A wind power tower, (b) Central lines of two cross weld lines (ground-truth), (c) Motion trail of the robot and (d) 3D information reconstruction of a tracked region of the weld lines. (For interpretation of the references to color in this figure legend, the reader is referred to the web version of this article.)

With the designed CSL sensor, we proposed a new laser stripe extraction approach and a new measurement calibration model, based on which the coefficients of the structured light planes can be estimated. Experiment results on the video sequences captured from a wall climbing robot platform show that the RMS error is within 0.407 mm, which can feed the requirement from practical applications.

Acknowledgments

References

[1] Carvalho E, Molina L, Freire E, Freire R, Luciano B. Fillet weld identification for automatic inspection of spherical tanks. In: Proceedings of IEEE international instrumentation and measurement technology conference proceedings, pp. 1–6; May 2007.

[2] Carvalho E, Luciano B, Freire R, Molina L, Freire E. Fault-tolerant weld line detection for automatic inspection of storage tanks based on distance and visual information fusion. In: Proceedings of IEEE international instrumentation and measurement technology conference proceedings, pp. 791–796; May 2009.

[3] Molina L, Carvalho E, Freire E, Montalvão-Filho J, Chagas F. A robotic vision system using a modified Hough transform to perform weld line detection on storage tanks. In: Proceedings of IEEE Latin American robotic symposium, pp. 45–50; 2008.

[4] Molina L, Freire R, Carvalho E, Freire E. A model-based fault-tolerant weld line detection for automatic Inspection of storage tanks using visual information and α–β filter. In: Proceedings of Latin American robotics symposium and intelligent robotic meeting, pp. 25–29; Oct. 2010.

[5] Wang X, Liang D, Zhang T. A robust vision based weld center finding method in automatic ultrasonic nondestructive test. In: Proceedings of IEEE international control and automation conference, pp. 162–165; May 2007.

[6] Zhang L, Jiao J, Ye Q, Han Z, Yang W. Robust weld line detection with cross structured light and Hidden Markov Model. In: Proceedings of IEEE international mechatronics and automation conference, pp. 1411–1416; Aug. 2012.

[7] Yoo WS, Na SJ. Determination of 3-D weld seams in ship blocks using a laser vision sensor and a neural network. J Manuf Syst 2003;22(4):340–7.

[8] Lee SK, Na SJ. A study on automatic seam tracking in pulsed laser edge welding by using a vision sensor without an auxiliary light source. J Manuf Syst 2002;21(4):302–15.

[9] Xu J, Xi N, Zhang C, et al. Real-time 3D shape inspection system of automotive parts based on structured light pattern. Opt Laser Technol 2011;43(1):1–8.

[10] Zhang R, Zhang X, Qin G, et al. Novel three-dimensional data conversion technique and profile measurement system for engine cylinder head blank. Opt Laser Technol 2012;45(7):697–701.

[11] Sun J, Liu Z, Zhao Y, et al. Motion deviation rectifying method of dynamically measuring rail wear based on multi-line structured-light vision. Opt Laser Technol 2013;50:25–32.

[12] Kowarschik R, Ku P, Schreiber W, et al. Adaptive optical three-dimensional measurement with structured light. Opt Eng 2000;39(1):150–8.

[13] Zhou F, Peng B, Cui Y, et al. A novel laser vision sensor for omnidirectional 3D measurement. Opt Laser Technol 2012;45.

[14] Bieri LS, Jacot J. Three-dimensional vision using structured light applied to quality control in production line. Proc. SPIE 2004;5457:463–71 (Apr.).

[15] Asakura H, Yamashita A, Kaneko T. 3-D measurement of an object by a mobile robot equipped with a laser range finder. In: Proceedings of the joint symposium between sister universities in mechanical engineering, pp. 107–110; Aug. 2004.

[16] Fu G, Corradi P, Menciassi A, Dario P. An integrated triangulation laser scanner for obstacle detection of miniature mobile robots in indoor environment. IEEE/ASME Trans Mechatron 2011;16(4):778–83.

[17] Ho G, Kim J. Model-based light stripe detection for indoor navigation. Opt Lasers Eng 2009;47(1):62–74.

[18] Xu D, Wang L, Tu Z, Tan. M. Hybrid visual servoing control for robotic arc welding based on structured light vision. Acta Autom Sin 2005;31(4):596–605.

[19] Wu Q, Su X, Song F. A pruning algorithm for the skeleton of line structure light pattern. J Sichuan Univ 2006;38(5):148–51.

[20] Sui L, Li B, Jiang Z. Research on method of laser knife center position extracting based on NURBS interpolation. Chin J Lasers 2003;30(10):933–6.

[21] Faugeras O. Three-dimensional computer vision: a geometric viewpoint. The MIT Press; 1993.

[22] Zhang Z. A flexible new technique for camera calibration. IEEE Trans Pattern Anal Mach Intell 2000;22(11):1330–4.

[23] More J. The Levenberg–Marquardt algorithm: implementation and theory. Numerical analysis. Berlin Heidelberg: Springer; 1978; 105–16.